Lab on a Chip

Accepted Manuscript

ROYAL SOCIETY OF CHEMISTRY

www.rsc.org/loc

Journal Name

ARTICLE

Received 00th January 20xx,

Accepted 00th January 20xx

DOI: 10.1039/x0xx00000x

www.rsc.org/

Bubble pump: Scalable strategy for in-plane liquid routing

Ali Oskooei[a] and Axel Günther[a,b]

We present an on-chip liquid routing technique intended for application in well-based microfluidic systems that require long-term active pumping at low to medium flowrates. Our technique requires only one fluidic feature layer, one pneumatic control line and does not rely on flexible membranes and mechanical or moving parts, thereby rendering it compatible with both elastomeric and rigid substrate materials and the associated scalable manufacturing processes. Directed liquid flow was achieved by an in-series configuration of two previously described gas-bubble enabled micro-valves (i.e. bubble gates) acting upon a liquid-filled channel. Only *one* time-dependent pressure signal is required for the upstream (active) bubble gate where it initiates a reciprocating bubble motion. The gas pressure of the downstream (passive) gate is time-constant and lower than the one applied on the active gate. In its resting state, the passive gate is closed and allows for downstream flow when the upstream pressure temporarily rises in response to the active gate's reciprocating bubble motion. We have designed, fabricated and consistently operated our bubble pump with a variety of working liquids for >72 hours at flow rates of 0-5.5µl/min, depending on the selected geometric dimensions, working fluids and actuation frequencies. The maximum operational pressure was 2.9 kPa -9.1 kPa depended on the interfacial tension of the working fluids. Attainable flow rates compared favorably with or exceeded those of available micropumps without the limitations pertaining to multilayer fabrication, biocompatibility, control and operation or substrate material elasticity. We achieved flow rate enhancements of 30-100% by operating two bubble pumps in tandem and demonstrated scalability of the concept in a multi-well format with 12 individually and uniformly perfused microchannels (variation in perfusion flow rate <7%). We envision the demonstrated concept to allow for the consistent on-chip delivery of a wide range of different liquids that may even include highly reactive or moisture sensitive solutions. Applications may include active flow control for analytical and point-of-care diagnostic devices, as well as the microfluidic perfusion culture of cells and organ-on-chip platforms.

1. Introduction

In the past two decades microfluidic and lab-on-a-chip technologies have shown significant promise in a wide range of applications such as: analytical[1-4] and diagnostic devices[5-8], platforms for chemical and material synthesis[9-13] and microphysiological systems[14-20]. Active flow control and sample delivery remain critical functions in microfluidic devices. External pumps (e.g., syringe pumps) have routinely been used to direct flow in microfluidic channels and are suitable for continuous flow microfluidic applications with typical fluid volumes of 1-50 ml. However, external pumps are often ill-suited for delivering large numbers of samples of minute volumes as required by many integrated lab-on-a-chip applications and chemical or biological screening tasks. Disadvantages of external pumps include: large size (e.g., the weight of a typical syringe pump exceeds one hundred times the weight of a typical microfluidic device), limited scalability, high cost, slow response time[21], and the large fluid dead volumes associated with external reservoirs and tubing that often exceeds the microchannel volume by at least one order of magnitude. It is therefore desirable, particularly for portable well-based analytical devices, to provide low-cost, easy-to-fabricate, and scalable approaches for flow control.

A large number of active on-chip pumping strategies have been suggested over the past decade[22,23]. These techniques have harnessed a wide range of physical and chemical phenomena to induce flow in microchannels including: pneumatically induced deflection of membranes[24-31], piezoelectricity[32-34], electrostatic effects[35-41], electrochemical reactions[42-46], thermo-pneumatic[47-49] and acoustic[50-55] effects. To date, the most widely used of these techniques are the pneumatic membrane pumps such as the peristaltic pump introduced by Quake's group[24,56,57]. As described by the schematic illustration in Fig. 1a, many of the flow control strategies developed to date include features that limit their utility in a range of applications. For instance most biological applications involving living cells or microorganisms are incompatible with high electrical voltages[58], high temperatures and electrochemical reactions. On the other hand, membrane

[a] Department of Mechanical and Industrial Engineering, University of Toronto, 5 King's College Road, Toronto, Ontario, M5S 3G8, Canada. Fax: +1-416-978-3356; Tel: +1-416-978-1282; E-mail: axel.guenther@utoronto.ca.
[b] Institute of Biomaterials and Biomedical Engineering, University of Toronto, 164 College Street, Toronto, Ontario, M5S 3G9, Canada

† Electronic supplementary information (ESI) available: Five videos and a supplementary document. See DOI: 10.1039/x0xx00000x

based strategies rely on the use of elastic materials that are susceptible to degradation when exposed to solvents or reactive fluids. For instance polydimethylsiloxane (PDMS) based micro-pumps are not compatible with organic solvents[59,60]. Many of the previously discussed techniques require complex multilayer fabrication and precise alignment that increase the fabrication cost. Therefore, consistent, programmable, scalable and substrate-independent delivery of small fluid volumes remains a critical requirement for well-based portable microfluidic devices (Fig. 1b).

We present an on-chip flow routing strategy that overcomes several of the aforementioned limitations through operation of a pair of "bubble gates" [61] in series. In our liquid routing technique the upstream bubble gate is active and serves as an actuator displacing a volume of the working liquid while the downstream bubble gate is passive and serves as a flow rectifier ensuring liquid flow in the downstream direction. Our devised technique requires only a single layer fabrication and does not require elastic substrate materials or moving parts and is therefore implementable in hard materials such as silicon[61]. It is also readily scalable without a need for additional controls or setup modifications. Figure 1b provides a conceptual illustration of a target microfluidic device for our devised strategy.

Details of the design and operation principle of our technique will be discussed in detail in Section 2. In Section 3 various configurations of the bubble pump including a single, parallel and scaled up configurations are investigated analytically and experimentally.

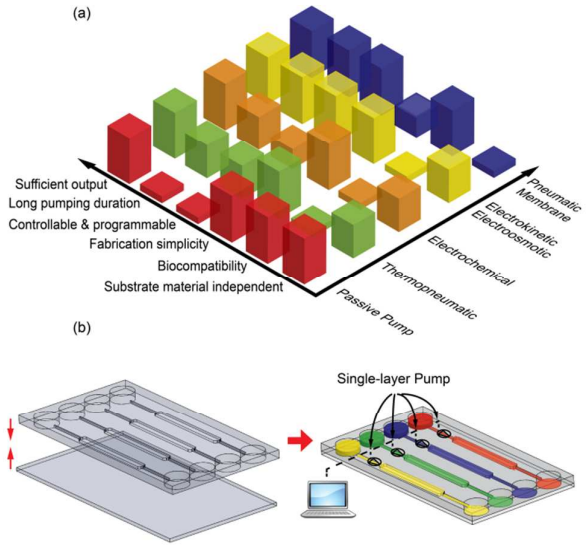

Figure 1. (a) Overview of different types of on-chip micropumps compared according to parameters affecting their utility. Different pumping techniques distinguished by colour. Sizes of bars represent qualitative score for each type of micropump. (b) Schematic illustration of a single layer well-based analytical device with on-chip sample routing strategy based on single layer fabrication and only one pneumatic actuation signal.

2. Experimental

2.1 Device design and experimental set up

The bubble pump consists of an in-series configuration of two previously described bubble gates [61]. Each bubble gate consists of a gas bubble that intercepts a liquid channel at a T-shaped junction and can allow or stop the liquid flow by precise control of the bubble movement inside the liquid channel. The bubble movement into the liquid channel is confined by means of two rows of closely packed micro-pillars that flank the T-junction. In our bubble pump, we employ an active bubble gate (i.e., the upstream gate) for liquid actuation and a passive bubble gate (i.e., the downstream gate) that serves as a flow rectifier allowing a net liquid flow in the downstream direction.

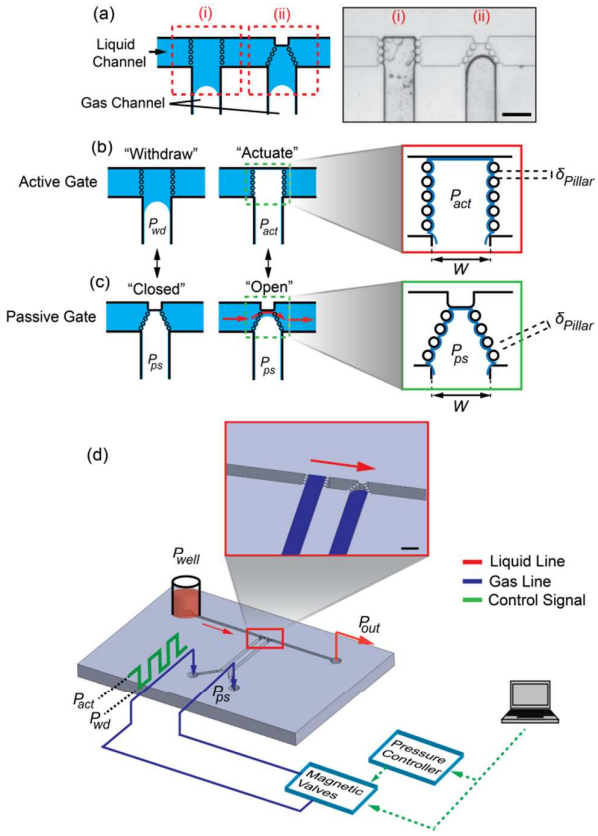

Figure 2. (a) Schematic illustration of the bubble pump design consisting of an in-series configuration of active (upstream) and passive (downstream) bubble gate forming a flow routing unit. Bright field micrograph showing bubble pump in operation. Scale bar 500µm. (b) Active bubble gate in "withdrawal" and "actuation" states along with enlarged view of active gate. Two arrays of micro-pillars limit bubble motion inside liquid channel to one degree of freedom perpendicular to the liquid channel. (c) Passive gate in its "closed" and "open" states as a result of withdrawal and actuation states of active gate. (d) Experimental setup employed for experiments with bubble pump. Liquid was displaced from inlet reservoir to the outlet using bubble pump. Refillable inlet reservoir and the outlet were at atmospheric pressure. All gas pressure levels were computer controlled and bubble pump was activated by applying a square wave pressure input at the inlet of active gate. Scale bar 500µm.

The design for the bubble pump is shown in Fig. 2a with the active bubble gate on the upstream (i.e. left) side and the

passive bubble gate on the downstream (i.e. right) side. To operate the pump the active gate is set in a reciprocating motion by alternating the gas pressure between a higher pressure level, P_{act}, and a lower pressure level, P_{wd}, as described in Fig. 2b. As shown in Fig. 2c the passive bubble gate is maintained at a constant pressure in its unperturbed "closed" state where it occupies the entire liquid channel cross section. During the actuation step, the active gate meniscus protrudes into the liquid channel displacing a volume of liquid and in turn, increasing the liquid pressure behind the passive gate which results in the opening of the passive gate. The brief opening of the passive gate allows a fraction of the displaced liquid volume to flow downstream. The passive gate rapidly returns to its resting "closed" state as the active gate withdraws from the liquid channel, hence, preventing back flow. As shown in Fig. 2c, the passive gate is designed with a tapered micro-pillar arrangement, a configuration that minimizes the contact area of the gas bubble with the liquid channel's top wall. The tapered configuration facilitates detachment of the meniscus from the upper wall during actuation. Other taper angles and contact areas were investigated and will be discussed in section 2.2. Figure 2d schematically illustrates the employed experimental setup. The working liquid was pipetted in the inlet well and collected at the outlet. Two gas lines with computer controlled gas pressures were involved in pumping of a working liquid from the inlet reservoir to the outlet. Only one control line generating a square wave pressure input with adjustable upper (P_{act}) and lower (P_{wd}) pressures and frequency was needed to pump the liquid from the inlet to the outlet. Details of flow control and delivery will be discussed in more detail in section 2.6.

Schematic illustrations and bright field micrographs in Fig. 3a show the bubble pump completing its three-step pumping cycle. The gas pressure for the passive gate was maintained constant at $P=P_{ps}$ in all steps of the cycle while the gas pressure for the active gate was alternated between a higher actuation pressure level of $P=P_{act}$ and a lower withdrawal pressure of $P=P_{wd}$. As shown in the pressure profiles in Fig. 3a, for successful operation of the bubble pump the actuation pressure must exceed the passive gate pressure and the withdrawal pressure must remain lower than the gas pressure for the passive gate, $P_{wd} \leq P_{ps} \leq P_{act}$.

2.2 Numerical simulation

Numerical simulations were performed using the modeling software, ANSYS (V14.5, Canonsburg, PA, USA), to investigate, compare and optimize different design configurations and to ensure that the adopted design will generate the maximum output in the desired direction when subjected to the operation cycle shown in Fig. 3a. We employed a volume of fluid (VOF) numerical model[62, 63] in ANSYS Fluent V14.5 to examine the pumping ability and achievable flow rates.

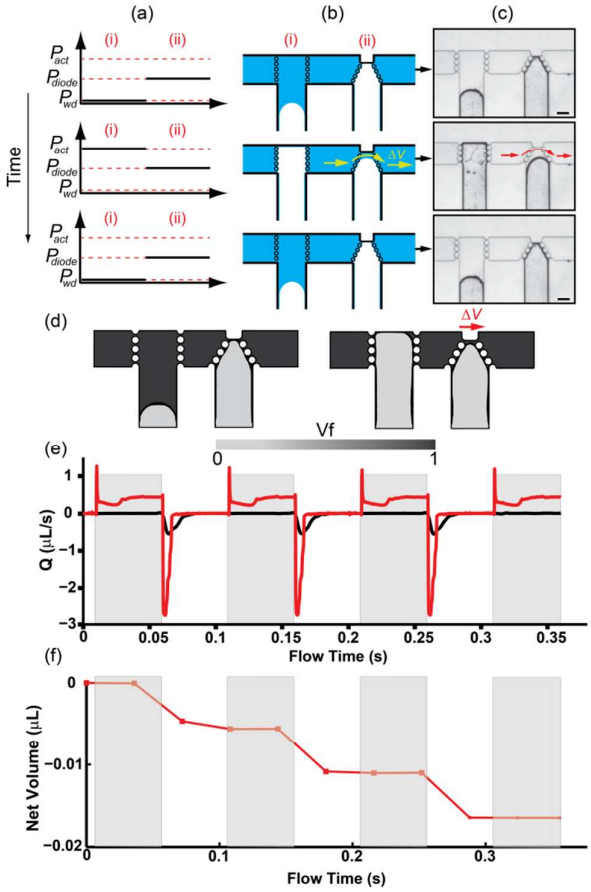

Figure 3. (a) Active and passive bubble gate pressures applied during one pumping cycle: (i) represents the active gate and (ii) represents the passive gate. (b) Schematic illustrations of bubble pump in its three-step pumping cycle (c) Bright field micrographs showing bubble pump in each step of its pumping cycle.(d) Numerically predicted air (light grey color) - ethyl alcohol (dark grey color) phase distributions during actuation and withdrawal steps. (e) Instantaneous flow rate computed at inlet (red) and outlet (black) of bubble pump for f=10Hz, P_{act}=700Pa, P_{wd}=0, P_{ps}=600Pa. (f) Net liquid volume pumped downstream obtained by integration of numerically predicted instantaneous flow rates. Scale bar 250μm.

We adopted a pressure-based, double precision, two-dimensional, transient VOF solver with pressure boundary conditions at the gas and liquid inlets and the liquid outlet. No-slip boundary condition was applied at the channel walls. The pressure inlet boundary condition for the active gate was a time-dependent boundary condition that was programmed as a user defined function (UDF) in C++ and implemented in FLUENT to model the square-wave pressure input for the active bubble gate. The numerically obtained gas (grey) and liquid (dark grey) phase distributions are shown in Fig. 3d. As shown in the figure, during actuation the passive gate opens partially allowing for the liquid to flow downstream. Figure 3e shows the time variation of liquid flow rate at the inlet (red line) and the outlet (black line) of the bubble pump in our model. A negative flow rate describes the desired liquid flow in the downstream direction, while a positive flow rate indicates reverse flow. As shown in Fig. 3e, the inlet flow rate periodically alternates between positive and negative values as the bubble pump completes its operating cycle shown in Fig.

3a. This sign alternation indicates that a fraction of the liquid volume displaced by the active bubble gate flows upstream while the remainder travels downstream towards the outlet. The wholly negative flow rate at the outlet of the bubble pump signifies a unidirectional flow in the downstream direction at all times. The plot in Fig. 3f shows the computed net liquid volume displaced by the bubble pump over time. The net displaced volume was determined by integration of the instantaneous flow rate at the outlet of the bubble pump. The volumetric flow rate produced by the bubble pump was determined from Fig. 3f to be approximately 3.6µl/min which agrees favourably with our experimental data for the same pumping frequency (i.e., 10Hz) and working fluids (i.e., ethanol and air).

Different bubble pump configurations were investigated numerically. Figure 4 demonstrates a numerical study of the three different passive gate geometries that we considered.

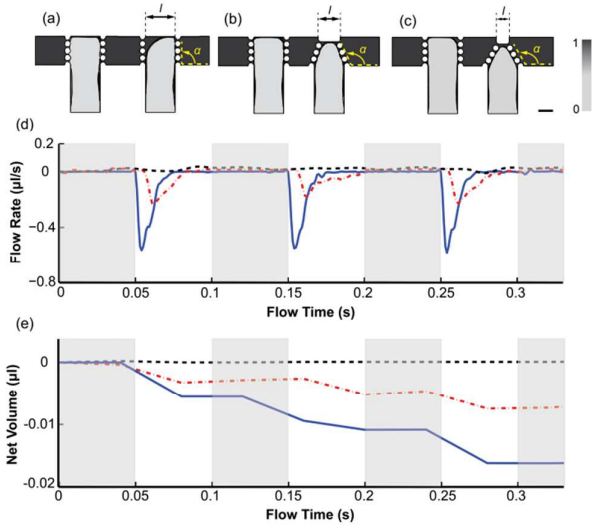

Figure 4. Numerically predicted volume fraction contours for three bubble pump designs with three different passive gate geometries: (a) α=90° and *l*=500µm (b) α=110° and *l*=330µm (c) α=120° and *l*=220µm (d) Flow rate with time at the outlet of bubble pump for three different geometries studied: α=90° and *l*=500µm (dashed line), α=110° and *l*=330µm (dash-dotted line) and α=120° and *l*=220µm (solid line). Design in (c) has the highest outlet flow rate for same pumping conditions (P_{act}=0.7kPa, P_{ps}=0.6kPa, *f*=10Hz).(e) Net volume displaced with time for designs in (a), (b) and (c) confirming that (c) displaces the largest volume followed by (b) configuration while (a) produces no net flow. Scale bar 250µm.

Figure 4a shows the numerically predicted volume fraction contour for the bubble pump with a passive gate geometry that is identical to the active gate with a pillar array taper angle (the angle between the micro-pillar array and the liquid channel) of *α=90°* and wall contact length of *l=500µm*. As shown in Fig. 4a, during actuation, the gas-liquid interface within the passive gate remains firmly attached to the downstream pillar array, rather than withdrawing from the liquid channel to allow for downstream flow. In designs shown in Fig. 4b and 4c the pillar arrays are tapered at angles of *α=110°* and *α=120°* and wall contact lengths are *l=330µm* and *l=220µm* respectively. Figure 4d shows the time-dependent volumetric flow rates produced by the three different pump designs. As indicated by the flow rate data, for the same operating pressures and frequency, the greater the taper angle, α, and the smaller the wall contact area, *l*, the higher the downstream flow rate will be. Figure 4e shows the net volume displaced by the three bubble pump designs over time confirming that the passive gate design in Fig. 4c delivers the highest displaced fluid volume while the design in Fig. 4a produces zero net flow. The higher flow rate for the design in Fig. 4c can be explained by more effective opening of the passive gate due to smaller wall contact area that results in a smaller disjoining force[64-66] ($F_{dj}=P_{dj}A_{contact}$) required to open the passive gate. Due to its superior flow rate output, we adopted the design in Fig. 4c in our experiments throughout this work.

2.3 Operational envelope

To explain the pumping mechanism of the bubble pump and to determine the pressure envelope for its successful operation we have employed the hydraulic circuit representation of the bubble pump shown in Fig. 5a. The bubble pump is connected to an inlet reservoir with a pressure of P_{well}. The pressure at the outlet of the bubble pump is denoted by P_{out}. In our experimental setup inlet and outlet were subjected to atmospheric pressure (i.e., zero gauge pressure).

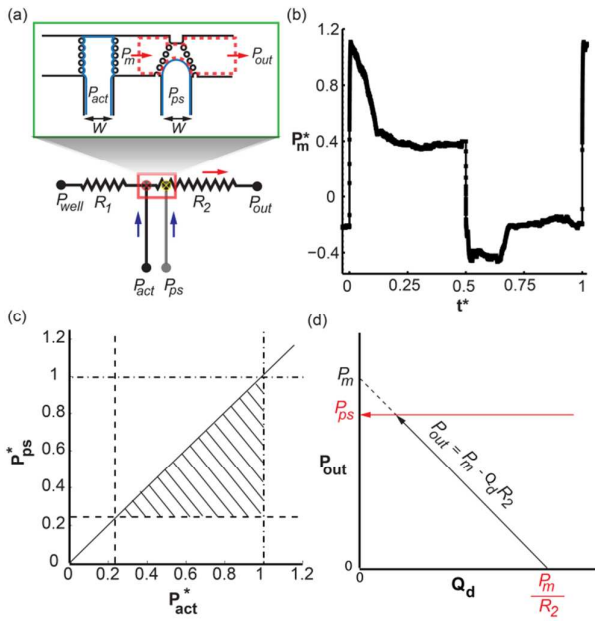

Figure 5. (a) Hydraulic circuit for the bubble pump. Liquid inlet is connected to a reservoir at $P=P_{well}$ while device outlet is at $P=P_{out}$. Flow resistance upstream of active bubble gate denoted by R_1 and resistance downstream of active bubble gate denoted by R_2. (b) Numerically obtained intermediate pressure, P_m, with time for one pumping cycle. P_m has been normalized with respect to P_{ps}, $P^*_m=P_m/P_{ps}$. Flow time normalized with respect to period of oscillations, $t^*=t/T_{total}$. (c) Operating pressure envelope for bubble pump is shown by hatched triangular area. All pressures are normalized with respect to maximum capillary pressure at which interface breakup occurs through micro-pillars (ΔP_{Pillar}). Both active and passive pressures must remain below maximum pressure (dash-dotted line) and above minimum pressure required to enter microchannel (dashed line). Active pressure must be greater than passive pressure (below the solid line). (d) Flow rate as a function of outlet pressure head. Flow rate decreases with increasing outlet pressure and bubble pump stops operating at an outlet pressure of P_{ps} when the passive gate no longer prevents backflow.

As discussed earlier the pressure of passive gate was maintained constant at P_{ps} while the active gate pressure oscillated between P_{act} and P_{wd}. P_{wd} was atmospheric (zero gauge) in the majority of our experiments and therefore, the active gate pressure oscillated between zero and P_{act}. The flow resistance before and after the active gate are denoted by R_1 and R_2 respectively.

During the actuation step, the active bubble gate acts as a piston driving the liquid towards the liquid channel where the displaced fluid volume is split in two fluid sub-streams one flowing upstream (Q_u), and the other flowing downstream (Q_d). Q_u is a backflow towards the inlet reservoir and Q_d is the desirable bubble pump output that flows past the passive gate and is collected at the outlet. The liquid pressure behind the passive gate inside the channel connecting the active and passive gates is denoted by P_m. The intermediate liquid pressure, P_m, is initially zero when the pump starts operating and as the active bubble gate begins oscillating and driving the liquid towards the liquid channel, P_m rises until it surpasses the passive gate pressure momentarily, $P_{ps}<P_m<P_{act}$. The elevated liquid pressure behind the passive gate results in the opening of the gate allowing a fraction of the displaced liquid volume (Q_d) to flow downstream. Figure 5b shows time variation of the intermediate pressure, P_m, during one pumping cycle obtained from numerical simulations. The pressures are normalized with respect to P_{ps} for a case where P_{act}=1.6 P_{ps}. It is noteworthy that to ensure successful bubble pump operation, P_m must surpass the passive gate pressure (P_{ps}) and therefore, the active gate pressure must exceed the passive gate pressure at all times, $P_{ps}<P_{act}$.

In order to understand and explain the flow rate delivered by the bubble pump, we assume a pressure driven flow along the flow passage depicted by the red dashed boundary in Fig. 5a. As shown in Fig. 5a the pressure along the flow passage decreases from P_m to P_{out} at the outlet. Therefore, the higher the intermediate pressure, P_m , the higher the bubble pump output is. The magnitude of P_m however is dependent on the actuation pressure (P_{act}) and the pressure of the passive gate (P_{ps}) and cannot be increased arbitrarily. The pressure in both the active and passive bubble gates is limited by ΔP_{Pillar}, the maximum capillary pressure the gas-liquid interface can withstand before it penetrates the liquid channel through the narrow gap between the micro-pillars. Therefore, the pressure difference across the interface must remain lower than ΔP_{Pillar} to ensure successful pumping without interface breakup. On the other hand, there is a lower limit for the gas pressure in the bubble gates imposed by the minimum capillary pressure required for the gas bubble to enter the channels leading to the bubble-pump. We denote this pressure with ΔP_{min}. The minimum and maximum capillary pressures are dependent on the bubble pump geometry and the working fluids:

$$\begin{cases}\Delta P_{Pillar} = 2\gamma\left(\frac{1}{\delta}+\frac{1}{H}\right)\\ \Delta P_{min} = 2\gamma\left(\frac{1}{w}+\frac{1}{H}\right)\end{cases} \rightarrow \frac{\Delta P_{min}}{\Delta P_{Pillar}} = \frac{\left(\frac{1}{w}+\frac{1}{H}\right)}{\left(\frac{1}{\delta}+\frac{1}{H}\right)} \quad (1)$$

where γ is the interfacial tension coefficient, H is the channel height and is constant throughout, δ is the gap size between the micro-pillars and w is the width of the gas channel. The ratio of the minimum capillary pressure to the maximum capillary pressure is purely geometrical as shown in Eqn.1 and is nearly 0.2 in all bubble pump devices tested in this work except for the design we employed for pumping of culture medium which will be discussed in detail in section 3.1.

Figure 5c shows the operation envelope for the bubble pump as a general guideline for acceptable interfacial pressure difference across the active (P_{act}) and passive bubble gates (P_{ps}). All pressures were normalized with respect to the maximum capillary pressure, ΔP_{Pillar}. As discussed earlier, both active and passive gate pressures must remain between the minimum and maximum pressures represented by dashed and dash-dotted lines in Fig. 5c respectively. Moreover, the pressure of the passive gate must remain lower than that of the active gate to ensure effective pumping. The hatched area in Fig. 5c represents the operation envelope for the bubble pump.

As discussed earlier during the actuation step the intermediate pressure, P_m, behind the passive bubble gate rises as the active bubble gate meniscus protrudes into the liquid channel and this elevated pressure results in opening of the passive gate and displacement of the working liquid towards the outlet. Assuming pressure driven flow through the flow passage starting immediately upstream of the passive gate and ending at the outlet (the conduit shown with the red dashed boundary in Fig. 5a) the resulting flow rate is obtained as:

$$Q_d = \frac{P_m - P_{out}}{R_2} \rightarrow P_m - P_{out} = R_2 Q_d \quad (2)$$

Following a similar process the upstream flow rate (i.e., the back flow) can be obtained as:

$$Q_u = \frac{P_m - P_{well}}{R_1} \quad (3)$$

From Equations 2 and 3 the ratio of downstream to upstream flow rate will be:

$$\frac{Q_d}{Q_u} = \frac{(P_m - P_{out})R_1}{(P_m - P_{well})R_2} \quad (4)$$

According to Eqn. 4, for a device with similar flow resistances before and after the active bubble gate and for similar pressures at the inlet and outlet the upstream and downstream flow rates are equal. This was confirmed by our numerical studies also.

Figure 5d shows the plot for Eqn. 2 indicating that the bubble pump output decreases with increasing outlet pressure. Mathematically speaking, it is expected from Eqn. 2 that the bubble pump stops pumping when the outlet pressure is equal to P_m. However this does not hold true in practice as the passive bubble gate will fail to perform its flow rectifying role when the outlet pressure approaches P_{ps} (red line in Fig. 5d). As a result the pressure head at the outlet of bubble pump

must remain well below the passive gate pressure for effective pumping.

2.4 Device fabrication

Devices were fabricated in PDMS (SYLGARD 184, Dow Corning Corporation, Midland, MI) using soft-lithography technique. As the first step to fabricate PDMS devices, a replica was made by photolithography on a microscope glass slide as the substrate. In order to fabricate the replica, a negative photoresist (SU8-2050, MicroChem, Newton, MA, USA) was spun on the glass slide and baked on a hotplate first at 65ºC and then at 95ºC. The baked photoresist was then covered with a photomask containing the design features and exposed to UV light. Following exposure to UV light through the photomask, the substrate was baked again on a hotplate at 65 and 95 degrees. After the post-exposure bake, the substrate was allowed to cool down before the unexposed photoresist was removed by immersing and shaking the substrate in photoresist developer solution (MicroChem, Newton, MA, USA) for ten minutes. The final replica fabrication step was to heat up the wafer at 150 degrees for five minutes to remove any liquid residues. Next, PDMS resin and curing agent were mixed and applied to the replica in a petri dish and degassed in a vacuum chamber (Model 280A, Fisher Scientific, ON, Canada).

The molded PDMS was heated in an oven at 80ºC for 30 minutes. The bubble pump devices were then cut and removed from the replica and the inlet and outlet holes were punched. The hole for the inlet well was nearly 3.2 mm (1/8 in) in diameter and the outlet holes were nearly 1.6 mm (1/16 in) in diameter. The microchip was then cleaned and placed in a Plasma Cleaner (Harrick, Ithaca, NY, USA) with a glass slide. Following exposure to oxygen plasma for 30 seconds, the treated surfaces were brought into contact to form an irreversible seal. A 3ml syringe (BD-Canada, Mississauga, ON, Canada) is cut to form a 1ml liquid reservoir and is then placed at the device inlet.

To ensure hydrophilic PDMS surface for measurements done with cell culture medium the devices were plasma bonded and were tested immediately after plasma treatment to ensure a wetting channel surface and formation of a lubricated interface.

2.5 Chemicals

Ethanol (100%, Commercial Alcohols, ON, Canada) was used as a representative for organic solvents and was used in characterization experiments. Mineral oil light grade (Bioshop Canada, Burlington, ON, Canada) was tested as a representative for oils and the resulting flow rate data were collected and are discussed in Section 3. RPMI 1640 culture medium (Life Technologies Inc., Burlington, ON, Canada) supplemented with fetal bovine serum (10%) and penicillin was used to verify utility of the bubble pump for mammalian cell culture applications. Air was used as the working gas in all experiments. All working fluids were prepared and applied at room temperature (~20 to 25ºC).

2.6 Flow delivery and control

Computer-controlled digital servo pressure controllers (Type 3110, Marsh Bellofram, Newell, WV, USA) that allowed precise pressure control (ε_p=0.005psi) via LabView (V12.0.1, National Instruments, Austin TX, USA) were employed to control the gas pressure levels for the active and passive bubble gates. The passive gate pressure was kept constant while there were two different pressure levels for the active gate for each of the actuation and withdrawal states. The pressure of the active gate was alternated between the two fixed pressure levels using an electromagnetic valve (The Lee Company USA, Westbrook, CT, USA) controlled using a LabView software. The withdrawal pressure level was atmospheric in all experiments except for experiments with culture medium. In case of culture medium pumping a slightly higher pressure than atmospheric was used to prevent abrupt withdrawal of the interface and foam formation. As a result, two pressure controllers were employed for culture medium pumping while all other experiments required only one pressure controller. All working liquids were delivered to the device by pipetting the liquid inside the inlet reservoir.

2.7 Imaging and image processing

Bright field microscopy was used to visualize the two phase flow inside the microfluidic devices. An inverted microscope (Eclipse TE-2000-S, Nikon, Japan) was used for visualization and imaging of the experiments. Images and videos were captured using a CCD camera (QImaging QICam Fast 1394, Surrey, BC, Canada) installed on the microscope.

3. Results and Discussion

3.1 Flow rate characterization

The bubble pump is similar to a macroscale plunger pump with the difference that it only includes one passive valve and the plunger stroke or the volume of the displaced fluid is variable unlike the mechanical plunger pump. Therefore, the flow rate delivered by the bubble pump is dependent on the stroke length (Δy) of the active bubble gate that acts as the piston in a plunger pump. In our bubble pump assuming a negligible film thickness, the displaced fluid volume, ΔV, can be written as:

$$\Delta V = \Delta y A_{ch} = U t_{wd} A_{ch} \quad (5)$$

where U is the withdrawal velocity of the interface and t_{wd} is the amount of time the active gate is withdrawing from the liquid channel drawing a liquid volume (ΔV) back into the active gate channel and A_{ch} is the cross-sectional area of the channel. Converting the displaced volume to the total flow rate produced by the active gate we can write:

$$\begin{cases} Q_{total} = Q_u + Q_d \rightarrow \frac{\Delta V}{T} = Q_u + Q_d \\ T = t_{wd} + t_{act} = 1/f \end{cases} \quad (6)$$

where Q_{total} is the total flow rate and T is the time period of the reciprocating motion of the active bubble gate including

the time it is withdrawing and the time it is actuating. Substituting for parameters in Eqn. 6 from Equations 2 to 5 we obtain:

$$\begin{cases} Ut_{wd}A_{ch}f = Q_d + xQ_d \\ x = \frac{(P_m - P_{well})R_2}{(P_m - P_{out})R_1} \end{cases} \quad (7)$$

Rearranging Eqn. 7, the net downstream flow rate of the bubble gate can be written as:

$$\begin{cases} Q_d = \frac{Ut_{wd}A_{ch}}{(1+x)(t_{wd}+t_{act})} = \frac{UrA_{ch}}{(1+x)(r+1)} = \frac{Ut_{wd}A_{ch}f}{(1+x)} \\ r = \frac{t_{wd}}{t_{act}} \end{cases} \quad (8)$$

where *r* is the ratio of the time the active bubble withdraws to the time it actuates.

To ensure utility of the bubble pump with different working fluids and to characterize the pumping performance we tested the bubble pump with different liquids and measured the flow rates produced. Flow rates were measured by measuring the volume of the liquid output over time. The schematic in Fig. 6a illustrates the experimental setup employed for flow rate measurement experiments. As shown in the schematic illustration, straight clear tubing with inner diameter of 1mm was fixed onto a ruler and connected to the outlet to allow for continuous measurement of the liquid volume exiting the pump. The bubble pump was allowed to operate at different combinations of t_{wd} and t_{act} (i.e., different frequency, *f*, and stroke size, *Δy*). Figures 6b to 6f present the experimental data for flow rate characterization of the bubble pump with air and ethanol as working fluids.

In Fig. 6b the flow rate data is plotted versus frequency for a case where the withdrawal time is kept constant at 300ms (i.e., constant stroke length, *Δy*) while the actuation time and as a result the operation frequency is varied. As shown in Fig. 6b the flow rate increases linearly with increased frequency. However there is a limit as to how low the actuation time can be decreased (i.e. the frequency increased) without compromising flow rate due to incomplete or partially-complete pumping cycles. The effect of partial or incomplete cycles can be seen towards the highest frequencies in the plot where the slope of the flow rate data begins to diminish. The initial linear behavior however is predictable according to Eqn. 8 when written in the format below with t_{wd} as a constant:

$$Q_d = \frac{Ut_{wd}A_{ch}f}{(1+x)} \quad (9)$$

Equation 9 represents the red dashed trend line in Fig. 6b with a constant slope for the frequencies where the bubble pump operates with complete pumping cycles.

Figure 6c shows the flow rate data plotted against the operation frequency for balanced operation cycles with equal withdrawal and actuation times (*r=1*). Substituting for *r* in Eqn. 8 we obtain the outlet flow rate as:

$$Q_d = \frac{UA_{ch}}{2(1+x)} \quad (10)$$

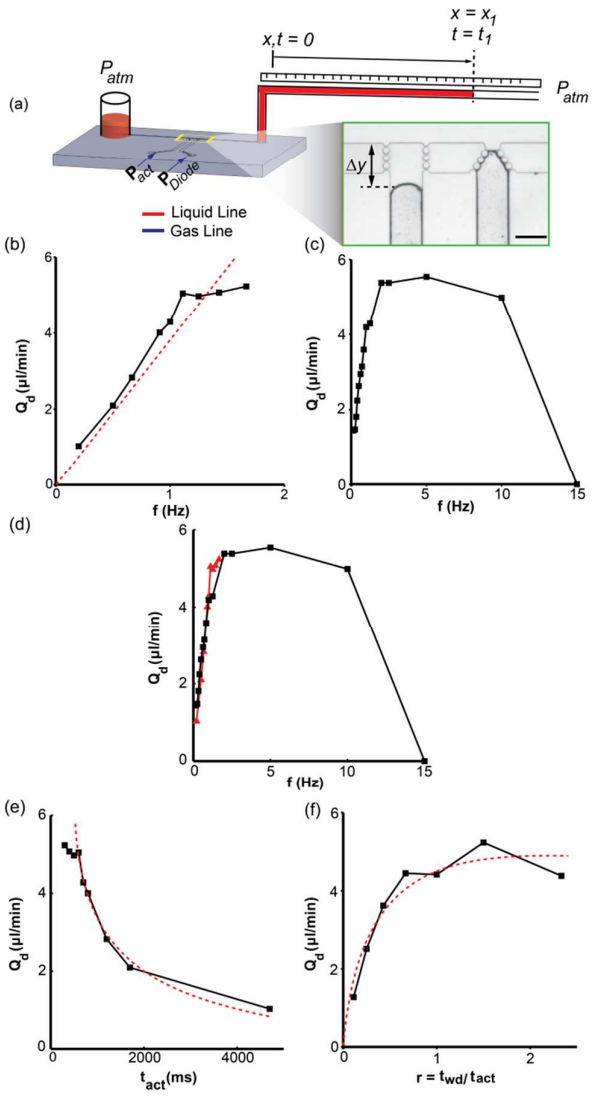

Figure 6. (a) Experimental setup employed to measure flow rate of bubble pump. Capillary of known inner diameter (1mm) was connected to the outlet to measure volume of displaced liquid over time. Ethanol and oil were used as working fluids for characterization experiments. (b) Measured flow rate plotted against actuation frequency with withdrawal time kept constant at 300ms. (c) Measured flow rate plotted against actuation frequency for pumping with balanced cycle when actuation and withdrawal times were equal (t_{wd}= t_{act}). (d) Superimposed flow rate-frequency data from (b) and (c). Agreement between pumping with balanced cycle (t_{wd}= t_{act}) and pumping with constant withdrawal time indicates that for low frequencies flow rate is independent of withdrawal time. (e) Measured flow rate plotted versus actuation time while keeping withdrawal time constant at 300ms. (f) Measured flow rate plotted against *r*= t_{wd}/t_{act}. Ratio *r* was varied while maintaining a constant frequency of 1Hz.

Equation 10 indicates that in the case where withdrawal and actuation times are equal flow rate is not a function of frequency. As shown in Fig. 6c, the independence of flow rate from frequency holds true for frequencies ranging over nearly an order of magnitude from frequency of two to ten. For frequencies higher than ten the active bubble gate fails to actuate as the time interval between actuation and withdrawal of the interface is too brief for the gas-liquid interface to respond to the pressure input and as a result the attainable

flow rate is zero. On the other hand, at frequencies lower than two the flow rate begins to decrease as the actuation and withdrawal times increase. At low frequencies (i.e., long withdrawal times) the gas-liquid interface has sufficient time to withdraw all of the available gas channel length on the device regardless of the frequency and as a result is similar to the case in Fig. 6b where the withdrawal time is constant and the flow rate decreases linearly with decreasing frequency. Figure 6d shows the flow rate data from Fig 6b and 6c superimposed. As seen in the superimposed plot the two data sets agree for low pumping frequencies (f<2Hz) for the reason discussed above.

In Fig. 6e flow rate is plotted versus actuation time (t_{act}) while maintaining the withdrawal time (i.e., pumping stroke length) constant at 300ms. As demonstrated by the data the flow rate decreases with increased actuation time as it reduces the pumping frequency while maintaining the displaced liquid volume in a single cycle (ΔV) constant. The red dashed trend line for the experimental data shown in Fig. 6e is predicted analytically by Eqn. 8 when written in terms of withdrawal and actuation times as below:

$$Q_d = \frac{Ut_{wd}A_{ch}}{(1+x)(t_{wd}+t_{act})} \quad (11)$$

The flow rate data presented in Fig. 6f point out the effect of varying values of withdrawal time to actuation time ratio, $r=t_{wd}/t_{act}$. As shown by the experimental data with increased r the flow rate initially increases sharply but the slope gradually declines until the output flow rate reaches a plateau. . The effect of varying r on flow rate can also be explained analytically by Eqn. 8 when written in terms of r:

$$Q_d = \frac{UrA_{ch}}{(1+x)(r+1)} \quad (12)$$

The red dashed trend line for the experimental data in Fig. 6f is predicted analytically by Eqn. 12 when plotted against r. At high values of r corresponding to extremely low actuation times the flow rate begins to drop as a result of partially-complete pumping cycles caused by the interface's inability to actuate long enough to travel the full length of the pumping stroke.

Microfluidic systems have been extensively used for cell culture and cell biology studies[67,68]. In order to demonstrate utility of the bubble pump for cell culture applications we conducted pumping experiments with a common mammalian cell culture solution consisting of RPMI 1640 culture medium supplemented with 10% FBS and penicillin. Our initial experiments with the original device dimensions (i.e., design of Fig. 4c) were hindered by occasional foaming of the culture medium due to the mechanical stresses caused by abrupt motion of the active bubble gate and high concentration of surfactants present in the culture medium. To enhance reliability of our pumping strategy with cell culture medium and solutions with high surfactant concentration we redesigned the bubble pump and reduced the gas channel width to one fifth of the original size and the liquid channel width to one half as shown in Fig. 7a.

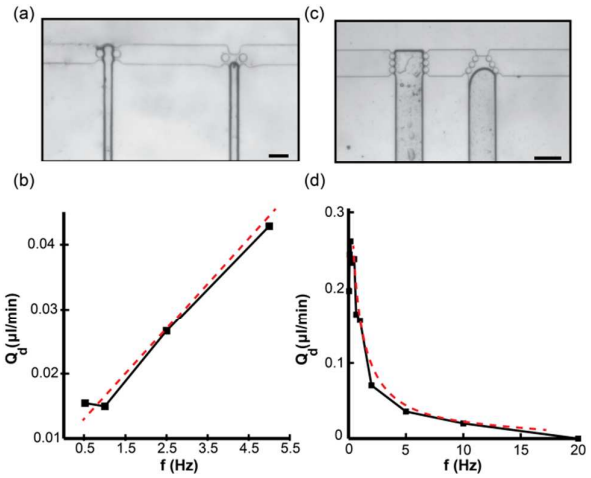

Figure 7. (a) Micrograph showing bubble pump in operation with working fluids of culture medium plus 10% fetal bovine serum (FBS) and air. Dimensions were reduced to ensure reliable long-term pumping for cell culture applications. Scale bar 250µm. (b) Flow rate versus actuation frequency for pumping with balanced cycle, t_{wd}= t_{act}, and working fluids of culture medium and air. (c) Bright field micrograph for bubble pump operating with working fluids of mineral oil and air. Scale bar 500µm. (d) Measured flow rate versus actuation frequency data for pumping with balanced cycle, t_{wd}= t_{act}, and working fluids of mineral oil and air.

The reduction in channel dimensions increased the interfacial tension and rigidity of the gas bubble and reduced the likelihood of interface breakup and foaming during bubble pump operation. To further reduce the likelihood of foam generation we limited the withdrawal distance of the active bubble gate by raising the withdrawal pressure (P_{wd}) slightly to a non-zero pressure unlike all previous experiments with other working fluids. These modifications resolved the foaming problem and reliable pumping was achieved for more than 72 hours of uninterrupted operation. The achievable flow rates, however, were reduced by the design and operational modifications as they decreased the displaced liquid volume. A flow rate of nearly 0.043µl/min (or 0.72nl/s) was the maximum flow rate achievable after modifications. For long term cell culture applications, however, high flow rates are not required as the flow rate is limited by the shear stress threshold that living cells can undergo[69,70]. Perfusion flow rates of below 0.1µl/min have commonly been used for culture medium delivery in microfluidic cell culture applications[71-73]. Figure 7b shows the flow rate data obtained for pumping with the culture medium. As seen in Fig. 7b flow rate increases linearly with pumping frequency as a result of our intentional maintenance of a constant stroke distance. Similar to the flow rate data in Fig. 6b the linear behavior for the flow rates in Fig. 7b can be explained by Eqn. 9.

In order to extend the utility of our bubble pump to applications involving high viscosity liquids we tested and characterised the bubble pump with light mineral oil. Figure 7c

shows the bright field image of the bubble pump operating with mineral oil and air as working fluids. The experimental flow rate data for pumping with mineral oil is presented in Fig. 7d. The flow rate data in Fig. 7d were acquired for pumping with a balanced cycle where the withdrawal and actuation times were equal (i.e. *r=1*). As shown in Fig. 7d, the bubble pump output increases rapidly with increased frequency and peaks at a maximum flow rate of nearly 0.26µl/min before starting to decline. The sharp decline in the flow rate for pumping with mineral oil occurs due to the high viscosity of the mineral oil slowing down the bubble movement during actuation which in turn results in partial actuation and a decreased flow output. It is noteworthy that the average flow rate produced with mineral oil (μ=23cP[74], Q_{avg}=3.27µl/min) as the working liquid was 19.2 times smaller than the average flow rate obtained with ethanol (μ=1.1cP[75], Q_{avg}=0.17µl/min), a ratio that is comparable with the ratio of viscosities (i.e., $Q_{Ethanol}/Q_{oil} \sim \mu_{oil}/\mu_{Ethanol}$). This observation further confirms our assumption of pressure driven flow in Eqn. 2 indicating that the output flow rate decreases with increasing flow resistance (R_2) as was the case in our experiments with mineral oil (i.e. increased viscosity results in increased flow resistance).

3.2 Parallel configuration and scalability

To enhance the flow output of the bubble pump we devised and investigated a configuration that consisted of two bubble pumps operating in parallel within the same liquid channel displacing the working liquid from an inlet reservoir towards the outlet. Figure 8a shows the schematic illustration for the parallel pump design and a bright field micrograph showing the pump in operation. Active and passive bubble gates for both pumps were connected to common gas inlets and as a result the controls required to operate the parallel pump were identical to those needed for a single bubble pump. The total flow rate output of the parallel pump configuration is the sum of flow rates for each individual pump ($Q_d=Q_1+Q_2$). Figure 8b shows the flow rate data for the parallel pump operating with working fluids of mineral oil and air (black line) superimposed with the flow rate data for a single bubble pump operating under the same conditions (red line). As shown in the plot the flow rate of the parallel pump is twice as high as that of a single bubble pump for frequencies higher than two. The flow rates of the parallel pump and the single pump converge as the pumping frequency decreases. At higher frequencies the stroke size of the bubble pump is small and the interface remains in the section of the gas channel that is identical to a single pump design as a result the volume displaced (i.e., flow rate produced) by the parallel pump is exactly two times that of a single pump. At low frequencies (i.e., long withdrawal times) however, the interface withdraws over a longer period of time traveling past the 90 degree bend in Fig. 8a that was designed differently from the single pump to allow for simultaneous control of both pumps. In low pumping frequencies, the difference in gas channel geometry for the parallel pump hinders the interface movement compared with the single pump and as a result the total volume displaced is less than twice that of a single gate. The flow rates for the parallel pump were however higher than that of a single gate for all pumping frequencies with both maximum flow rates and the average flow rate for the parallel pump being thirty percent higher than that of a single pump.

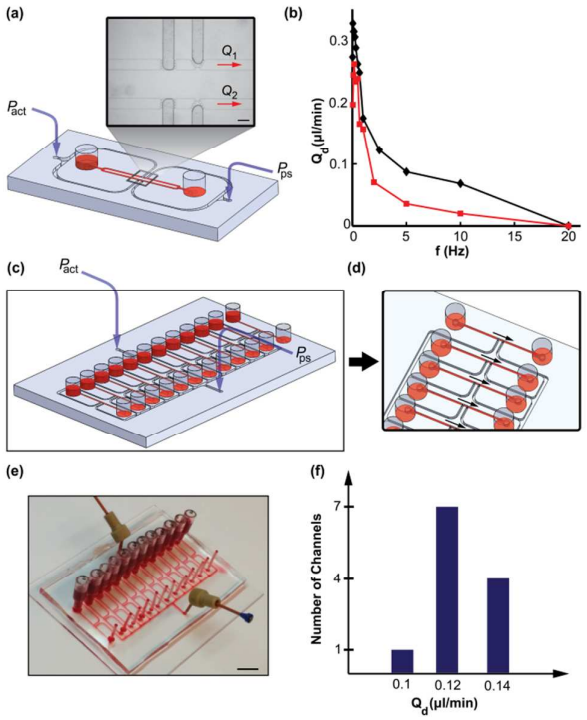

Figure 8. (a) Schematic illustration showing a parallel bubble pump configuration with two bubble pumps working in parallel in the same liquid line pumping the liquid from inlet well towards outlet. Bright field micrograph shows parallel pump in operation. Scale bar 500µm. (b) Measured flow rate data versus frequency for parallel pump configuration (♦) superimposed with those from single bubble pump (■) with working fluids of mineral oil and air. (c) Schematic illustration of scaled-up pumping device with twelve independent liquid channels. The working liquid is fed into twelve inlet wells each connected to an independent microchannel with a bubble pump displacing inlet liquid towards an outlet. All twelve active gates are controlled by a single pneumatic control line while all passive gates are connected to a common gas input. (d) Schematic illustration showing the close-up for structure of scaled-up pumping device. (e) Photograph of scaled-up pumping device with channels filled with red dye (f) Flow rate distribution across twelve microchannels on scaled-up pumping device operated with mineral oil and air at *f*=0.5Hz. Scale bar 1cm.

To demonstrate utility of the bubble pump in applications where a large number of concurrent processes take place such as in biological culture or drug screening we developed and tested a well-based scaled up device incorporating the bubble pump. Figure 8c shows the schematic illustration of the scaled up device. As shown in Fig. 8d the device consists of twelve independent microchannels each connected to an independent inlet well, a bubble pump and an independent outlet. Each of the twelve bubble pumps consists of an active and a passive gate. Similar to the parallel pump, all active and passive gates were connected to a common active and passive inlet respectively and therefore the controls required to operate all twelve pumps were identical to those needed to operate a single bubble pump. The twelve inlet wells were

filled with the working liquid (mineral oil) and the bubble pumps were started by setting the active gates in a reciprocating motion. We successfully controlled all twelve pumps with a single control line with minimal functional variation across the twelve pumps. The active gates demonstrated a consistent stroke length and oscillation timing across all twelve channels (See ESI movie 5). The histogram in Fig. 8f shows the flow rate distribution for the twelve microchannels. The data show an average flow rate of 0.13µl/min and a standard deviation of 0.01µl/min across the twelve microchannels, a seven percent deviation from the mean flow rate. The variation in flow rates is due to the slight variations in the stroke size caused by nonlinearities in the interface movement.

Conclusions

We presented an on-chip "bubble-pump" liquid routing strategy that tackles some of the unresolved problems associated with state of art microfluidic flow control techniques. Designed to deliver long term, low to medium flow rates in well-based integrated microfluidic platforms, our technique requires only a single feature layer, is independent of substrate material elasticity, biocompatible and scalable with no additional controls required. The bubble pump consists of an in-series configuration of two bubble gates, an active one upstream and a passive one downstream. We employed numerical and analytical models along with experimental studies to characterize operating conditions and pumping behaviour. We tested the bubble pump with ethanol, mineral oil and a cell culture medium. We believe the demonstrated pumping concept to be widely applicable for a wide range of (wetting) liquids with different viscosities and surface tensions. We uninterruptedly operated single-channel bubble pumps for more than 72 hours at the maximum flow rates of 5.5µl/min (ethanol), 0.26 µl/min (mineral oil) and 0.043 µl/min (cell culture medium). A 30-100% increase in flow rate was observed for a tandem bubble pump configuration that consisted of two bubble pumps in parallel. Scalability of the pumping strategy was demonstrated in a configuration that accommodated twelve bubble pumps. The array of bubble pumps was operated by only one common control signal and produced uniform flow rates with only a seven percent variation in between channels. The data in this paper were obtained from soft lithographically patterned devices. Even though experimental evidence has yet to be provided, we expect the presented bubble pump design to be compatible with a wide range of substrate materials beyond PDMS and with scalable commercial device manufacturing processes. The latter may include hot embossing and injection molding in thermoplastics, and deep reactive ion etching in silicon/glass and promise to overcome some of the challenges associated with the scalable manufacturing of microfluidic devices in PDMS.

Acknowledgements

We acknowledge an Alexander Graham Bell Canada Graduate Scholarship from the Natural Sciences and Engineering Research Council of Canada (AO), the Wallace G. Chalmers Chair of Engineering Design (AG), NSERC Discovery, Discovery Accelerator and Strategic Projects program awards, a Connaught Innovation Award and an Ontario Early Researcher Award. Device microfabrication was carried out at the CFI/ORF funded Centre for Microfluidic Systems in Chemistry and Biology (University of Toronto, Toronto, ON). We thank Dr. Milad Abolhasani for discussions.

References

1 P. Neuži, S. Giselbrecht, K. Länge, T. J. Huang and A. Manz, *Nature reviews Drug discovery*, 2012, **11**, 620-632.
2 C. T. Culbertson, T. G. Mickleburgh, S. A. Stewart-James, K. A. Sellens and M. Pressnall, *Analytical Chemistry*, 2013, **86**, 95-118.
3 P. Neužil, C. Campos, C. Wong, J. Soon, J. Reboud and A. Manz, *Lab on a Chip*, 2014, **14**, 2168-2176.
4 M. L. Kovarik, D. M. Ornoff, A. T. Melvin, N. C. Dobes, Y. Wang, A. J. Dickinson, P. C. Gach, P. K. Shah and N. L. Allbritton, *Analytical Chemistry*, 2012, **85**, 451-472.
5 C. Rivet, H. Lee, A. Hirsch, S. Hamilton and H. Lu, *Chemical Engineering Science*, 2011, **66**, 1490-1507.
6 X. Mao and T. J. Huang, *Lab on a Chip*, 2012, **12**, 1412-1416.
7 M. S. Akram, R. Daly, F. da Cruz Vasconcellos, A. K. Yetisen, I. Hutchings and E. A. Hall, in *Lab-on-a-Chip Devices and Micro-Total Analysis Systems*, Springer, 2015, pp. 161-195.
8 C. D. Chin, V. Linder and S. K. Sia, *Lab on a Chip*, 2012, **12**, 2118-2134.
9 P. M. Valencia, O. C. Farokhzad, R. Karnik and R. Langer, *Nat Nano*, 2012, **7**, 623-629.
10 T. W. Phillips, I. G. Lignos, R. M. Maceiczyk, A. J. deMello and J. C. deMello, *Lab on a Chip*, 2014, **14**, 3172-3180.
11 K. S. Krishna, Y. Li, S. Li and C. S. S. R. Kumar, *Advanced Drug Delivery Reviews*, 2013, **65**, 1470-1495.
12 S. Marre and K. F. Jensen, *Chemical Society Reviews*, 2010, **39**, 1183-1202.
13 L. Zhang and Y. Xia, *Advanced Materials*, 2014, **26**, 2600-2606.
14 B. Xiong, K. Ren, Y. Shu, Y. Chen, B. Shen and H. Wu, *Advanced Materials*, 2014, **26**, 5525-5532.
15 E. K. Sackmann, A. L. Fulton and D. J. Beebe, *Nature*, 2014, **507**, 181-189.
16 R. Gorkin, J. Park, J. Siegrist, M. Amasia, B. S. Lee, J.-M. Park, J. Kim, H. Kim, M. Madou and Y.-K. Cho, *Lab on a Chip*, 2010, **10**, 1758-1773.
17 J. Yu, J. Zhou, A. Sutherland, W. Wei, Y. S. Shin, M. Xue and J. R. Heath, *Annual Review of Analytical Chemistry*, 2014, **7**, 275-295.
18 K. N. Han, C. A. Li and G. H. Seong, *Annual Review of Analytical Chemistry*, 2013, **6**, 119-141.
19 J. Hu, S. Wang, L. Wang, F. Li, B. Pingguan-Murphy, T. J. Lu and F. Xu, *Biosensors and Bioelectronics*, **54**, 585-597.
20 W. Jung, J. Han, J.-W. Choi and C. H. Ahn, *Microelectronic Engineering*, 2015, **132**, 46-57.
21 Y. J. Kang and S. Yang, *Lab on a Chip*, 2012, **12**, 1881-1889.
22 C. K. Byun, K. Abi-Samra, Y.-K. Cho and S. Takayama, *Electrophoresis*, 2014, **35**, 245-257.
23 D. Laser and J. Santiago, *Journal of Micromechanics and Microengineering*, 2004, **14**, R35.
24 M. A. Unger, H. P. Chou, T. Thorsen, A. Scherer and S. R. Quake, *Science*, 2000, **288**, 113-116.

25 W. H. Grover, A. M. Skelley, C. N. Liu, E. T. Lagally and R. A. Mathies, *Sensors and Actuators B: Chemical*, 2003, **89**, 315-323.
26 W. Zhang, S. Lin, C. Wang, J. Hu, C. Li, Z. Zhuang, Y. Zhou, R. A. Mathies and C. J. Yang, *Lab Chip*, 2009, **9**, 3088-3094.
27 H. Chun-Wei, H. Song-Bin and L. Gwo-Bin, *Journal of Micromechanics and Microengineering*, 2006, **16**, 2265.
28 N. Sundararajan, D. Kim and A. A. Berlin, *Lab on a Chip*, 2005, **5**, 350-354.
29 M.-H. Wu, S.-B. Huang, Z. Cui, Z. Cui and G.-B. Lee, *Biomedical Microdevices*, **10**, 309-319.
30 H. Lai and A. Folch, *Lab on a Chip*, 2011, **11**, 336-342.
31 J. Kim, M. Kang, E. C. Jensen and R. A. Mathies, *Analytical Chemistry*, 2012, **84**, 2067-2071.
32 H. T. G. v. Lintel, F. C. M. v. d. Pol and S. Bouwstra, *Sensors and Actuators*, 1988, **15**, 153-167.
33 D. C. Roberts, L. Hanqing, J. L. Steyn, O. Yaglioglu, S. M. Spearing, M. A. Schmidt and N. W. Hagood, *Microelectromechanical Systems, Journal of*, 2003, **12**, 81-92.
34 L. Saggere, N. W. Hagood, D. C. Roberts, H. Q. Li, J. L. Steyn, K. Turner, J. A. Carretero, O. Yaglioglu, Y. H. Su, R. Mlcak, S. M. Spearing, K. S. Breuer and M. A. Schmidt, 2000.
35 B. Kim, S. Yoon, K. Lee and H. Sung, *Exp Fluids*, 2009, **46**, 85-95.
36 D. Lastochkin, R. Zhou, P. Wang, Y. Ben and H.-C. Chang, *Journal of Applied Physics*, 2004, **96**, 1730-1733.
37 K. Yang and J. Wu, *Biomicrofluidics*, 2008, **2**, -.
38 L. Olesen, H. Bruus and A. Ajdari, *Physical Review E*, 2006, **73**, 056313.
39 M. Lian and J. Wu, *Applied Physics Letters*, 2009, **94**, -.
40 H.-C. Yeh, R.-J. Yang and W.-J. Luo, *Physical Review E*, 2011, **83**, 056326.
41 A. Wego and L. Pagel, *Sensors and Actuators A: Physical*, 2001, **88**, 220-226.
42 B. Sebastian, T. Björn, O. Wouter and B. Piet, *Journal of Micromechanics and Microengineering*, 2000, **10**, 498.
43 I. F. Vasile, K. K. James and D. J. Harrison, *Journal of Micromechanics and Microengineering*, 2003, **13**, S164.
44 F. Sassa, K. Morimoto, W. Satoh and H. Suzuki, *Electrophoresis*, 2008, **29**, 1787-1800.
45 J. Nestler, A. Morschhauser, K. Hiller, T. Otto, S. Bigot, J. Auerswald, H. F. Knapp, J. Gavillet and T. Gessner, *Int J Adv Manuf Technol*, 2010, **47**, 137-145.
46 S. H. Chiu and C. H. Liu, *Lab Chip*, 2009, **9**, 1524-1533.
47 K. Handique, D. T. Burke, C. H. Mastrangelo and M. A. Burns, *Analytical Chemistry*, 2001, **73**, 1831-1838.
48 C. G. Cooney and B. C. Towe, *Sensors and Actuators A: Physical*, 2004, **116**, 519-524.
49 W. K. Schomburg, R. Ahrens, W. Bacher, S. Engemann, P. Krehl and J. Martin, 1997.
50 M. B. Dentry, J. R. Friend and L. Y. Yeo, *Lab on a Chip*, 2014, **14**, 750-758.
51 P.-H. Huang, N. Nama, Z. Mao, P. Li, J. Rufo, Y. Chen, Y. Xie, C.-H. Wei, L. Wang and T. J. Huang, *Lab on a Chip*, 2014, **14**, 4319-4323.
52 L. Schmid, A. Wixforth, D. Weitz and T. Franke, *Microfluid Nanofluid*, 2012, **12**, 229-235.
53 M. V. Patel, I. A. Nanayakkara, M. G. Simon and A. P. Lee, *Lab on a Chip*, 2014, **14**, 3860-3872.
54 A. Hickerson, D. Rinderknecht and M. Gharib, *Exp Fluids*, 2005, **38**, 534-540.
55 A. I. Hickerson and M. Gharib, *Journal of Fluid Mechanics*, 2006, **555**, 141-148.
56 F. K. Balagaddé, L. You, C. L. Hansen, F. H. Arnold and S. R. Quake, *Science*, 2005, **309**, 137-140.
57 R. Gómez-Sjöberg, A. A. Leyrat, D. M. Pirone, C. S. Chen and S. R. Quake, *Analytical Chemistry*, 2007, **79**, 8557-8563.
58 A. LaLonde, M. F. Romero-Creel and B. H. Lapizco-Encinas, *Electrophoresis*, 2014, DOI: 10.1002/elps.201400331, n/a-n/a.
59 J. N. Lee, C. Park and G. M. Whitesides, *Analytical Chemistry*, 2003, **75**, 6544-6554.
60 R. Dangla, F. Gallaire and C. N. Baroud, *Lab on a Chip*, 2010, **10**, 2972-2978.
61 A. Oskooei, M. Abolhasani and A. Gunther, *Lab on a Chip*, 2013, **13**, 2519-2527.
62 V. Cristini and Y.-C. Tan, *Lab on a Chip*, 2004, **4**, 257-264.
63 C. W. Hirt and B. D. Nichols, *Journal of Computational Physics*, 1981, **39**, 201-225.
64 B. V. Derjaguin and N. V. Churaev, *Journal of Colloid and Interface Science*, 1977, **62**, 369-380.
65 B. V. Derjaguin and N. V. Churaev, *Journal of Colloid and Interface Science*, 1978, **66**, 389-398.
66 B. V. Derjaguin and N. V. Churaev, *Journal of Colloid and Interface Science*, 1974, **49**, 249-255.
67 M.-H. Wu, S.-B. Huang and G.-B. Lee, *Lab on a Chip*, 2010, **10**, 939-956.
68 I. Meyvantsson and D. J. Beebe, *Annual Review of Analytical Chemistry*, 2008, **1**, 423-449.
69 J. T. Keane, D. Ryan and P. P. Gray, *Biotechnology and Bioengineering*, 2003, **81**, 211-220.
70 J. B. Joshi, C. B. Elias and M. S. Patole, *The Chemical Engineering Journal and the Biochemical Engineering Journal*, 1996, **62**, 121-141.
71 P. J. Hung, P. J. Lee, P. Sabounchi, R. Lin and L. P. Lee, *Biotechnology and Bioengineering*, 2005, **89**, 1-8.
72 L. M. Przybyla and J. Voldman, *Proceedings of the National Academy of Sciences of the United States of America*, 2012, **109**, 835-840.
73 F. Moledina, G. Clarke, A. Oskooei, K. Onishi, A. Günther and P. W. Zandstra, *Proceedings of the National Academy of Sciences of the United States of America*, 2012, **109**, 3264-3269.
74 C. A. Stan, S. K. Y. Tang and G. M. Whitesides, *Analytical Chemistry*, 2009, **81**, 2399-2402.
75 J. Liu, C. Zhu and Y. Ma, *Journal of Chemical & Engineering Data*, 2011, **56**, 2095-2099.